RESEARCH ARTICLE

Key Points:
- Six of the eight strongest surface cold pools, from 300 total, occur during convectively suppressed conditions with a dry midtroposphere
- Cold pools help explain why cumulus congestus are common in the Tropics
- A constrained cloud-resolving model simulation has realistic rain rates but too much rain evaporation in the boundary layer

Correspondence to:
A. Chandra and P. Zuidema,
arun.acsharma@gmail.com;
pzuidema@miami.edu

Moisture Distributions in Tropical Cold Pools From Equatorial Indian Ocean Observations and Cloud-Resolving Simulations

Arunchandra S. Chandra[1] , **Paquita Zuidema[1]** , **Steven Krueger[2]** , **Adam Kochanski[2]** , **Simon P. de Szoeke[3]** , **and Jianhao Zhang[1]**

[1]Department of Atmospheric Sciences, Rosenstiel School of Marine and Atmospheric Science, University of Miami, Miami, FL, USA, [2]Department of Atmospheric Sciences, University of Utah, Salt Lake City, UT, USA, [3]College of Earth, Ocean, and Atmospheric Sciences, Oregon State University, Corvallis, OR, USA

Abstract The near-surface characteristics of approximately 300 convective cold pools over the equatorial Indian Ocean are studied using surface meteorological variables from two equatorial Indian Ocean sites, radar imagery, and constrained cloud-resolving simulations. The observed temperature drop at cold pool onset is typically accompanied by a drying and a decrease in moist static energy, signifying air transport from above the boundary layer through precipitation-induced downdrafts. The decrease in the surface water vapor mixing ratio is more pronounced for stronger temperature drops. Composites reveal a slight enhancement in moisture coincident with a slight enhancement in temperature prior to the cold pool frontal temperature drop. The slight enhancements occur prior to a gust of increased surface winds, suggesting that the immediate cause is wind convergence. A statistical analysis combined with a focus on selected case studies is consistent with a view that the strongest cold pools occur in intermediate column water vapor paths with drier midtropospheres. Such conditions are more likely to occur during convectively suppressed phases of the Madden-Julian Oscillation, when cold pool mesoscale organization facilitates the ability of cumulus congestus to reach the middle troposphere. Cold pools thus help explain why tropical cumulus congestus are common. Cloud-resolving simulations capture realistic rain rates and surface wind changes (and thereby surface fluxes). The evolution in the model near-surface moisture field is unrealistic, however, with an erroneous moisture enhancement inside the cold pool edge that is attributed to rain evaporation. This supports a further focus on the model representation of cold pool frontal dynamics and mixing.

Plain Language Summary Cold pools of air develop near the surface over the ocean when it rains. This colder air can move along the surface because it is denser and cause new raining clouds to form. They help modify the types of clouds and convection present over the tropical oceans, and their depiction in climate models may help improve climate model simulations of tropical climate. In this study we use observations of cold pools, combined with radar imagery, to confirm that cold pools are more pronounced when the middle of the atmosphere, between 2 and 5 km, is also drier. Cold pools, because they help support updrafts, can also help explain why seemingly isolated clouds reaching ~5 km, are relatively common in the Tropics. Modeling simulations have instead focused on how anomalous moisture near the surface from previous convection, through, for example, rain evaporation, may spawn more convection. We find that in one cloud-resolving simulation, the rain evaporation is too much, leading to an unrealistic moisture distribution. This may explain why to date the understanding of cold pool processes through models and observations have not always agreed.

1. Introduction

Rain falling from a convective cloud, entering into an unsaturated boundary layer, will partially evaporate and generate with it a cold downdraft. This colder air can then fan out horizontally as a density current, demarcated through a gust front. This displaces and mixes with the surrounding warmer ambient boundary layer air. The developing cold pool of air continues to increase its mass through turbulent entrainment at the cold pool top, aided at times by gentle subsidence above the cold pool. In this manner a cold pool of air forms and grows near the surface. In the Tropics, interest in oceanic cold pools as a means for modifying air-sea exchange has existed since at least the Global Atmospheric Research Program Atlantic Tropical Experiments

in the early 1970s (Robert et al., 1981). Cold pools continue to receive scrutiny as an integral process affecting tropical cloud and precipitation mesoscale organization (Feng et al., 2015; Genio et al., 2015; Ruppert & Johnson, 2015; Zuidema et al., 2017). Better model cold pool representations may help establish a more realistic tropical environment within coupled climate models (Genio et al., 2012; Grandpeix & Lafore, 2010; Maloney & Hartmann, 2001; Rio et al., 2013). Dedicated remote sensing capabilities also enable more comprehensive characterizations (e.g., Rowe & Houze, 2015).

Convection is highly influenced by the subcloud moist static energy, more appropriately represented by the equivalent potential temperature (θ_e; Kingsmill & Houze, 1999), so that understanding how the surface θ_e is affected by cold pool processes is important for understanding subsequent convection. Early observational work relates decreases in the surface θ_e to rain rate, with θ_e decreasing once rain rates averaged over the rain catchment area exceed 2 mm/hr (Barnes & Garstang, 1982). Since the θ_e decrease reflects downdraft air originating from a higher altitude that almost always possesses a lower θ_e, with mixing with environmental air likely to occur along the way, the link between the atmospheric cold pool, the originating convection, and the accompanying thermodynamic profiles becomes of interest. The air within cold pools is also strongly affected by the recovery to ambient conditions. Cold pool recovery processes reflect the combined influences of surface fluxes from possibly cooled ocean surfaces (Pei et al., 2018) and entrainment and subsidence at the cold pool top (e.g., de Szoeke, 2018). While these processes are also important, they are not the focus of this study, which is on the impact of the initial convective downdrafts.

Some observations and modeling studies place the altitude of the undiluted downdraft air at 1–2 km or just above the boundary layer (Kingsmill & Houze, 1999; Torri & Kuang, 2016). The originating altitude can extend higher, up to 3–4 km if the θ_e profile only varies a little (de Szoeke et al., 2017) or if significant mixing is also occurring along the way (Schiro & Neelin, 2018). Air brought down from drier midtroposphere should correlate with stronger maximum decreases in the subsequent cold pool specific humidities and thereby θ_e, all else equal. This behavior is evident in the tethered balloon observations discussed in Addis et al. (1984) and in models (Jeevanjee & Romps, 2015). Other influences on the properties of the downdraft air include the saturation of the preexisting near-surface air, the amount of lateral entrainment, which is affected by the amount of cloud clustering (Feng et al., 2015; Mapes et al., 2017; Schlemmer & Hohenegger, 2014, 2016), and asymmetries in the environmental wind shear profile (Feng et al., 2015; Li et al., 2014; Zuidema et al., 2012). In concert, these findings support the importance of the environmental humidity at 2- to 4-km altitude for establishing downdraft characteristics but also make clear that the connection is not always clear or direct nor that the correlation between cold pool strength and midtropospheric humidity is necessarily statistically significant.

In this study, we connect the convective downdraft properties to the convection type and free-tropospheric moisture and discuss their relation to the Madden-Julian Oscillation (MJO) phase, using observations from the Dynamics of the MJO field campaign (DYNAMO; Yoneyama et al., 2013). A further aim of this study is to examine moisture variations in cloud-resolving model simulations that have been constrained by large-scale DYNAMO analyses. This is motivated by the intrigue that significant modeling research highlights an increase in surface moisture near the inside edge of a cold pool, (Langhans & Romps, 2015; Tompkins, 2001; Torri & Kuang, 2016) rather than the decrease often seen in observations (Zuidema et al., 2017).

2. Data Sets and Methodology

The cold pools are characterized using near-surface meteorological time series from two equatorial Indian Ocean sites, namely, Gan Island, located within the low-lying Addu atoll at 0.6° S and 73.2° E, and the research vessel *RogerRevelle*, located approximately 700 km to the east of Gan Island at 80° E, equator. Corresponding cloud-resolving simulations centered on each site provide the basis for the observational modeling intercomparison. More details on both the observations and model simulations follow.

2.1. Data Sets: Observations

The Gan Island measurements span 4 October through 31 December 2011 and primarily stem from an Atmospheric Radiation Measurement (ARM) ARM Mobile Facility (AMF) deployed as part of the ARM MJO Investigation Experiment (AMIE; Long et al., 2011). The surface meteorological measurements are reported every minute at an altitude of approximately 1 m. Air temperature measurements are accurate to 0.1 K, water vapor mixing ratio (q_v) to 0.2 g/kg, wind speeds to 0.1 m/s, and pressure to 0.15 hPa. One-minute rain rate measurements from an optical rain gauge are accurate to 0.1 mm/hr. Complementary measurements come from a 35-GHz K-band zenith-pointing cloud radar (KAZR), a three-frequency microwave radiometer (channels at

23.8, 30, and 89 GHz) providing column water vapor (CWV) path and liquid water path estimates, a ceilometer to detect cloud base, and a tipping-bucket rain gauge. All the instruments are located within 50 m of each other. The KAZR radar provides time-height depictions of the clouds above the surface cold pools at a vertical and time resolution of 30 m and 4 s, with radar reflectivities sensitive to −25 dBZ at 10 km (Chandra et al., 2015). The three-dimensional structure of convection is inferred from C-band (5.5-cm wavelength) Shared Mobile Atmospheric Research and Teaching Radar (SMART-R; Feng et al., 2014) imagery. The SMART-R single polarimetric Doppler radar is sensitive to −21 dBZ at a distance of 10 km and was located 8.61 km northwest of the KAZR. The SMART-R radar 10-min scanning pattern included, importantly, a directed range-height-indicator scan over the KAZR, corresponding to an azimuth angle of 147° relative to the SMART-R. The surveillance scan occurs at a 0.5° elevation angle and a range of 300 km. For local context in our selection of case studies, reference is also made to the daily summaries available at www.atmos.washington.edu/~houze/DYNAMO-AMIE/, which include analyses by the NCAR S-Pol radar, a 10-cm dual-polarization radar.

The *Roger Revelle* research vessel was on station from 30 September through 20 October 2011 and again from 7 November through 7 December 2011. The *Revelle* flux tower measured air temperature and humidity at 15 m above sea level and the vector wind at ~20 m above sea level. The sea temperature is measured at 0.1-m depth and adjusted for ocean cool skin and diurnal warm layer effects to represent the surface (Fairall, Bradley, Godfrey, et al., 1996). Turbulent flux computations are adjusted to a 10-m height using the COARE version 3.5 bulk aerodynamic formula (Fairall, Bradley, Rogers, et al. 1996; Fairall, Bradley, Godfrey, et al. 1996) based on Monin-Obukhov flux-gradient similarity. Other ship measurements include downwelling solar and longwave infrared radiative fluxes, optical rain gauge measurements, and liquid water path and water vapor path retrievals from a two-channel microwave radiometer. All measurements are analyzed at 1-min resolution.

Reference is also made to the realtime multivariate MJO index (or phase; Wheeler & Hendon, 2004). This seasonally independent index describes the evolution of the MJO along the equator using a pair of empirical orthogonal functions based on the near-equatorially averaged 850- and 200-hPa zonal winds and satellite-observed outgoing longwave radiation data. At Gan Island and the *Revelle*, the large-scale convectively organized time periods typically occur during MJO phases 1–3 (Gottschalck et al., 2013). These contain mesoscale cloud systems with large stratiform components that contain their own mesocirculations and span hundreds of kilometers. The less organized, more convectively suppressed time periods typically coincide with MJO phases 4 through 8 (Gottschalck et al., 2013). These are more likely to contain cumuli that can still reach deep into the troposphere but lack thick cirrus (e.g., Powell & R. A. Houze Jr, 2013; Riley et al., 2011). Cold pools have received more attention during the convectively suppressed time periods.

2.2. Data Sets: Simulations

The cloud-resolving simulations rely on the System for Atmospheric Modeling (SAM; Khairoutdinov & Randall, 2003, 2006). The domain size is 256 km by 256 km, with a cloud-resolving 1-km horizontal grid spacing and 67 vertical levels total. The simulations adopt a *single-column model* approach (Randall et al., 1996) in which a doubly periodic model domain is considered to represent a global climate model grid column. The large-scale vertical and horizontal advective tendencies of temperature and water vapor mixing ratio that would be produced by the convergence of fluxes from adjacent global climate model columns are instead specified from large-scale forcing data sets developed for this study. These rely on a constrained variational objective analysis (Xie et al., 2004; Zhang & Lin, 1997; Zhang et al., 2001, 2016) in which an average of the European Center for Medium Weather Forecasting analyses centered at each site (the ARM mobile facility and the *Revelle*) over a diameter of 300 km are constrained with surface rainfall rates estimated from the Tropical Rainfall Measurement Mission. The surface conditions are established, at Gan, by nearby daily Optimally Interpolated Sea Surface Temperatures (Banzon et al., 2016; Reynolds et al., 2007), and, at the *Revelle*, by the measured sea surface temperatures.

SAM is a nonhydrostatic numerical model that uses an anelastic dynamical core. Its prognostic thermodynamic variables are liquid-ice water static energy, total nonprecipitating (cloud water/ice) and total precipitating water (rain/snow/graupel). A two-moment microphysics scheme predicts the mixing ratios and number concentrations of cloud water, cloud ice, rain, snow, and graupel (Morrison et al., 2005). The two independent moments for each species allows for a more flexible representation of the evolution of the particle size distributions and thus, in principle, an improved capacity to simulate the microphysical processes affecting downdrafts. The Morrison scheme is known to produce relatively strong cold pools due to pronounced subcloud evaporation (e.g., Li et al., 2015). Solar and infrared radiative fluxes interact with clouds and the surface as well as the atmosphere and provide radiative heating rates. A new turbulence closure named Simplified

Higher Order Closure (SHOC; Bogenschutz & Krueger, 2013) prognoses the subgrid-scale turbulent kinetic energy and relates it and the eddy length scales to the turbulence length scale. The subgrid-scale condensation and buoyancy fluxes are diagnosed from an assumed joint density distribution. Additional moments required by the closure are also diagnosed. The turbulent surface fluxes are based on Monin-Obukhov similarity using the observed sea surface temperatures and the simulated atmospheric properties at the lowest model level. SAM-SHOC has the ability to realistically represent many boundary layer cloud regimes in cloud-resolving models with horizontal grid sizes of 0.5 km or larger (Bogenschutz & Krueger, 2013).

The SAM model near-surface air temperatures, water vapor mixing ratios, surface winds, and fluxes are saved at each grid point at 5-min resolution, with the time series sampled at 16 evenly spaced grid points for the statistical comparison. The lowest near-surface model grid spans 100 m of altitude, so that near-surface values correspond to a mean 50-m altitude. Diagnosis of the radiosondes indicates that in undisturbed conditions the boundary layer is typically well mixed up to 600 m. In such a boundary layer, the surface layer profiles of potential temperature and water vapor mixing ratio are nearly uniform above 5-m altitude, with a potential temperature difference between 5- and 50-m altitude that is typically less than 0.1 K (Fu et al., 1995). This justifies the comparison of the lowest-level model fluxes to the values calculated from the observations.

2.3. Cold Pool Identification

Cold pools, by definition, can be characterized through the temperature drops defining their edges. In the observations, a 5-min running-mean smoothing is applied to the original 1-min time series, to match the 5-min time resolution of the model output. The smoothed 5-min time series are further filtered using a square Haar wavelet (Percival & Walden, 2000) before identifying the beginning of the temperature drop. The maximum temperature at the beginning of the temperature drop signifies the beginning of the cold pool frontal passage, and the minimum temperature detected thereafter signals the end. The cold pool frontal passage is normalized to span 20 min, corresponding to the approximate median width of the cold pool front (Figure 6 in de Szoeke et al., 2017).

Time series can be subject to conditional sampling biases: It is not clear where, along the larger spatial boundary of a cold pool, the measurement is made (e.g., Tompkins, 2001). The connection of the individual cold pool to the parent convection is also not always clear, especially in cases of merged cold pools, as cold pools are more likely to occur near other cold pools. This is evident in Figure 1, wherein approximately four fifths of the temperature drops occur after rain is documented in the previous hour at the surface, rather than simultaneously or slightly later. For this reason, only those cold pools for which no rain occurs for 1 hr prior to the cold pool passage are selected, to reduce modification of the air prior to the cold pool passage by a different rain cell. This selection criterion is not rigorous, as cold pools can be frequent enough to lower the daily mean surface temperature (de Szoeke et al., 2017).

A further choice must be made regarding the temperature drop threshold used to indicate a cold pool passage, as more cold pools are detected using a weaker temperature threshold. The length of the Haar wavelet filter width applied to the smoothed time series is another subjective choice. The filter width is half the full width of the Haar window, and longer wavelet time intervals tend to reduce the number of weak cold pools detected (Figure 2). When the additional requirement of no rain prior for 1 hr is imposed, the number of detected cold pools decreases markedly, more so for the weaker cold pools. The most pronounced cold pools take the longest to develop, at more than 10 min, but the number of cold pools detected saturates after 15 min independent of the chosen temperature threshold.

Based on Figure 2, the cold pool selection criteria are chosen to be a temperature decrease of 0.4 K within a square Haar wavelet full-width window of 10 min, combined with a requirement of no rain for 1 hr prior to the temperature drop. The temperature maximum at the start of the temperature drop identifies the beginning, and the subsequent temperature minimum, its end. These criteria identify 193 cold pools at Gan island, and 103 at the *Revelle*. These criteria are more stringent than that imposed in de Szoeke et al. (2017), whose analysis is based on 215 cold pools detected at the *Revelle*, more than twice as many as are examined here. This is primarily because we exclude cases preceded by rain. The selection criteria do not necessarily adequately capture every single cold pool. Experimentation with other choices did not lead to significantly different interpretations of the data. In the case studies explored within section 5, two additional cold pools that are preceded by rain, as examples of a particular behavior.
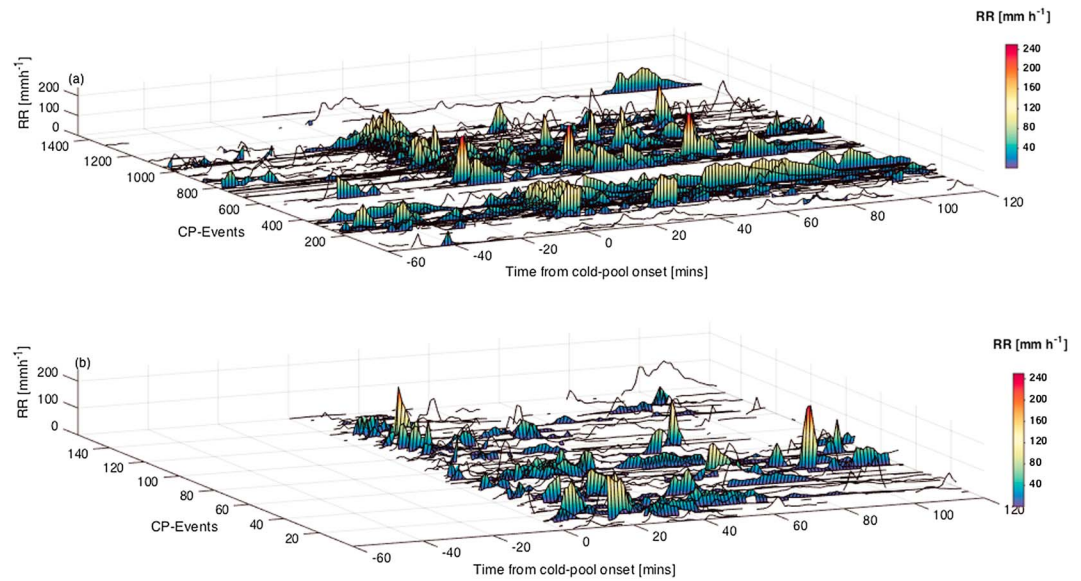
Figure 1. (a) Rainrates (RRs) associated with individual cold pools (CPs) at Gan Island identified using a temperature decrease of 0.3 K applied to air temperature time series smoothed using a 5-min running mean only and (b) further restricted to those with no rain within 1 hr prior of the temperature decrease.

3. Characteristics of Observed Cold Pools

A time series of the local near-surface air temperature, sea surface temperature, and rain rates for the full DYNAMO time period along with the daily maximum surface cold pool strength ($T_{max} - T_{min}$) provides context for evaluating the cold pools from the two sites (Figure 3). Gan Island experienced more and heavier rain, along with more and stronger cold pools, than the *Revelle*. This is consistent with significant variability in local MJO convection, also noticed in larger-scale radar analyses (Xu et al., 2015). A strong diurnal variability is evident in the air temperature at Gan Island, reflecting heating of the underlying land (atoll) surface. The diurnal variability at Gan Island does not alias into the shorter-term cold pool statistics, and no overall statistically significant night-day differences are evident at either location, in cold pool frequency or strength (not shown). This does not necessarily imply that diurnal cycles do not exist in specific convective regimes (e.g., Ruppert & Johnson, 2015), only that our aggregated data set does not resolve them. The 1–14 October and 10–17 November time periods, extensively studied in Ruppert and Johnson (2015) and Rowe and Houze (2015) and referenced further throughout this study, are outlined in Figure 3.
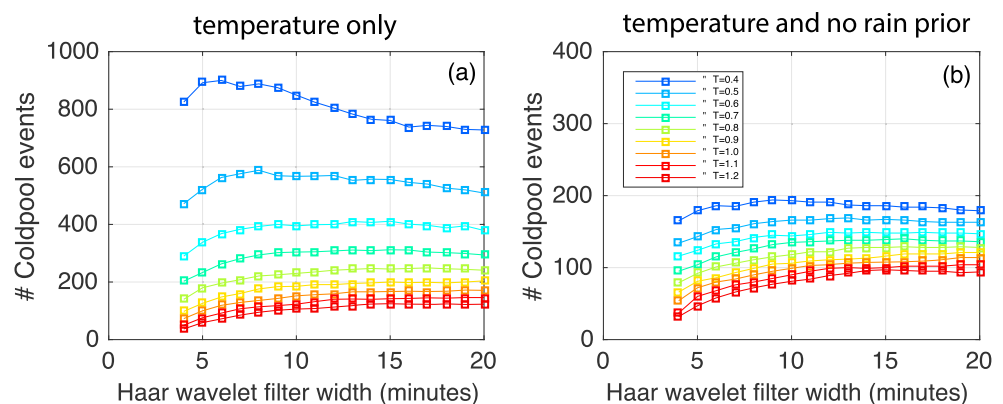

Figure 2. (a) The number of cold pools at Gan Island as a function of the Haar wavelet filter width and temperature drop. (b) Same as (a) but further restricted to cold pools with no rain within 1 hr prior of the temperature decrease.
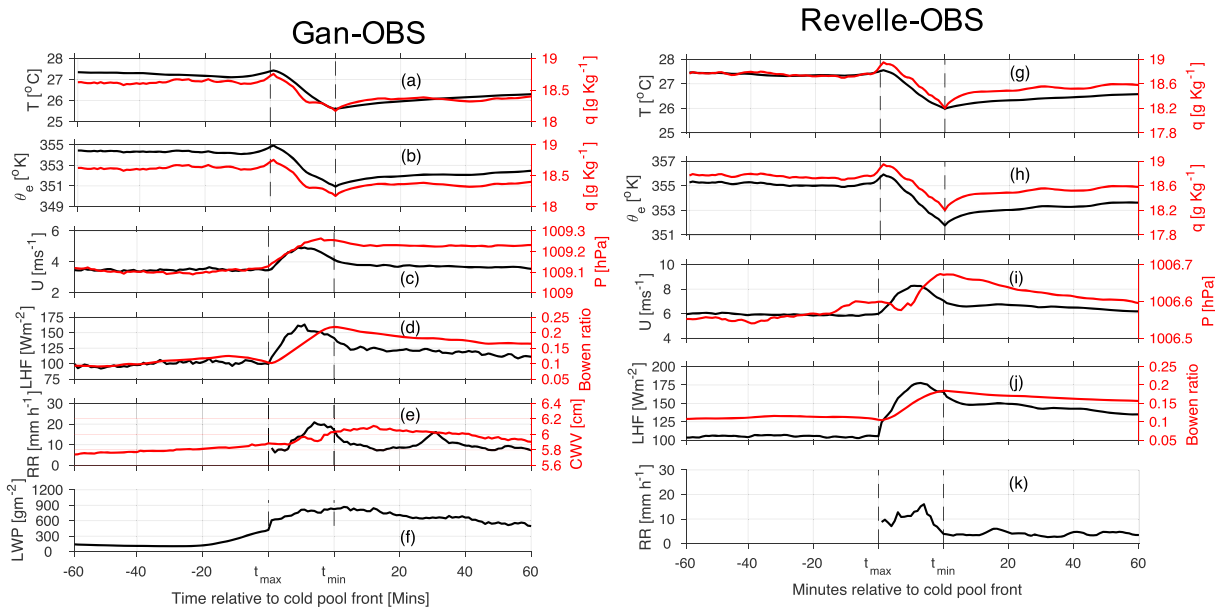
Figure 3. Time series at Gan Island (top) and the *Revelle* (bottom) of the smoothed 5-min surface air temperatures (thin gray lines) and their daily mean values (pink line), along with the daily mean sea surface temperature (red line; Optimally Interpolated Sea Surface Temperature averaged over 5° centered boxes), two measures of rain rate: optical rain gauge (thin dark-blue lines) and tipping bucket (thin light-blue line, only at Gan), and daily mean values of the CWV path (dark-black line). The daily minimum air temperatures are indicated by grey circles whose diameters are proportional to the daily maximum cold pool strength ΔT ($T_{max} - T_{min}$; the proportionality constant is not quantified). The MJO phase is indicated at the top of each panel. Cold pool cases detailed further in Table 1 are labeled with red numbers (top panel), also used within Figure 10. The black boxes outlined in dashes correspond to time periods discussed in Ruppert and Johnson (2015) and Rowe and Houze (2015). CWV = column water vapor; MJO = Madden-Julian Oscillation; SST = sea surface temperature.

3.1. Composites

The cold pool composites for both sites (Figure 4) indicate a slight temperature increase of approximately 0.1 K near the beginning of the cold pool front accompanied by an increase in the water vapor mixing ratio (q_v) of approximately 0.25 g/kg, corresponding to an increase in the equivalent potential temperature (θ_e) of 0.5 K. These precede a more robust temperature decrease of ~1.5 K and decrease in q_v of ~1 g/kg, for a decrease in θ_e of 4 K. Mean pre-cold-pool-onset winds are stronger at the *Revelle* than at Gan Island (6 vs. 3.5 m/s), as are the wind speed increases (2 vs. 1.5 m/s), which may reflect land friction at Gan, but in both composites the wind speed increase occurs after the slight increases in q_v and θ_e, and during the passage of the temperature drop. The temporal structure of the latent heat fluxes is set by that of the wind speeds, with a slightly higher initial increase at the *Revelle* (~75 vs. ~60 W/m²). The concurrent presence of rain is not one of the selection criteria for a cold pool, but their connection is nonetheless explicit within the composite, with the rain rates tending to reach their maximum toward the end of the cold pool frontal passage. This is more obvious at Gan. At Gan, the maximum wind speed occurs slightly ahead of the maximum rain rate, consistent with the idea of a gust front that is moving faster than the environmental surface wind, while at the *Revelle* the two maxima are more closely located in time. This may reflect the presence of stronger cold pool dynamics at Gan (Figure 3). At both sites, the recovery is slow in all the surface variables, exceeding the 1-hr post-cold front time window shown, with the exception of the winds and fluxes. Similar features are seen in Figure 5 of de Szoeke et al. (2017) using a less conservative protocol for identifying cold pools.

Further perspective is provided by sorting the cold pools according to their temperature decrease, from small to large (Figure 5). Although the individual cold pools are highly variable, a trend can be seen in which stronger temperature decreases are accompanied by stronger decreases in θ_e, which primarily reflect drying of the

Figure 4. Cold pool composite based on 193 cold pools at Gan Island (a–f) and 103 at the *Revelle* (g–k), from one prior to 1 hr past the cold pool frontal passage, the latter normalized to a 20-min time interval. (a, g) Air temperature (black) and water vapor mixing ratio (red). (b, h) Water vapor mixing ratio (red) and equivalent potential temperature (black). (c, i) Surface wind speed (black) and surface pressure (red). (d, j) LHFs (black) and the Bowen ratio (surface heat fluxes/LHFs; red). (e, k) RR (black) and CWV (red, [e] only). (f) LWP. CWV = column water vapor; LHF = latent heat flux; LWP = liquid water path; OBS = observation; RR = rain rate.

surface air (the latter not shown). Less clearly, the wind speeds and surface pressures increase concurrently as a function of the cold pool temperature drop. The plot convention does not well delineate the slight increases in temperature, q, and θ_e evident in the composites before the temperature drop constituting the cold pool front (Figure 4). More cold pools were sampled at Gan than at the *Revelle*, and more of them had large temperature and moisture decreases, consistent with Figure 3.

4. Relationship of Cold Pools to Column Moisture

Cold pools are hypothesized to be a key process within shallow-to-deep convection transitions, such as the 7–14 October and 11–15 November 2011 time periods outlined in Figure 3 (Rowe & Houze, 2015; Ruppert & Johnson, 2015). Dry midlevel tropospheres coexist with increasing column-integrated moisture and significant rainfall during these times (Ciesielski et al., 2017; Zhang et al., 2018). The convectively suppressed time periods at the two sites coincide statistically with MJO phases 4–8 (Gottschalck et al., 2013). Gan Island radiosondes composited by MJO phases indicate that MJO phases 5 and 6 are also characterized by low θ_e val-

Table 1
Individual Cold Pool Events at Gan, Most With Surface Drying Exceeding 2 g/kg, Sorted Approximately by Their Temperature Decrease From Largest to Weakest

Case	Date	UTC (hr)	MJO phase	Remarks
1*	31 Oct	04.28	3	Squall line with ice, 6-hr cold pool recovery, Figure 8
2*	8 Dec	08.48	5	Cloud line reaching 5 km, Figure 9d
3	15 Dec	10.96	4	Cold pool convection reaching 3 km
4	2 Dec	09.26	5	3-km convection, followed by subsequent event 1.5 hr later
5*	3 Dec	14.10	5	Cold pool convection reaching 6 km, Figure 9c
6	10 Oct	10.40	8	Two consecutive cold pools
7*	14 Oct	12.56	8	Cold pool convection reaching 6km, rain evaporation maintains θ_e prior to cold pool, Figure 9b
8*	23 Nov	11.38	2	Convective cell embedded in stratiform precipitation, Figure 9a

Note. The corresponding case numbers are included in Figures 3 and 7. The 10 and 14 October cases fall within the time period studied within Rowe and Houze (2015) and Ruppert and Johnson (2015). Asterisks next to the case number indicate that these cases are described further in the text. MJO = Madden-Julian Oscillation.
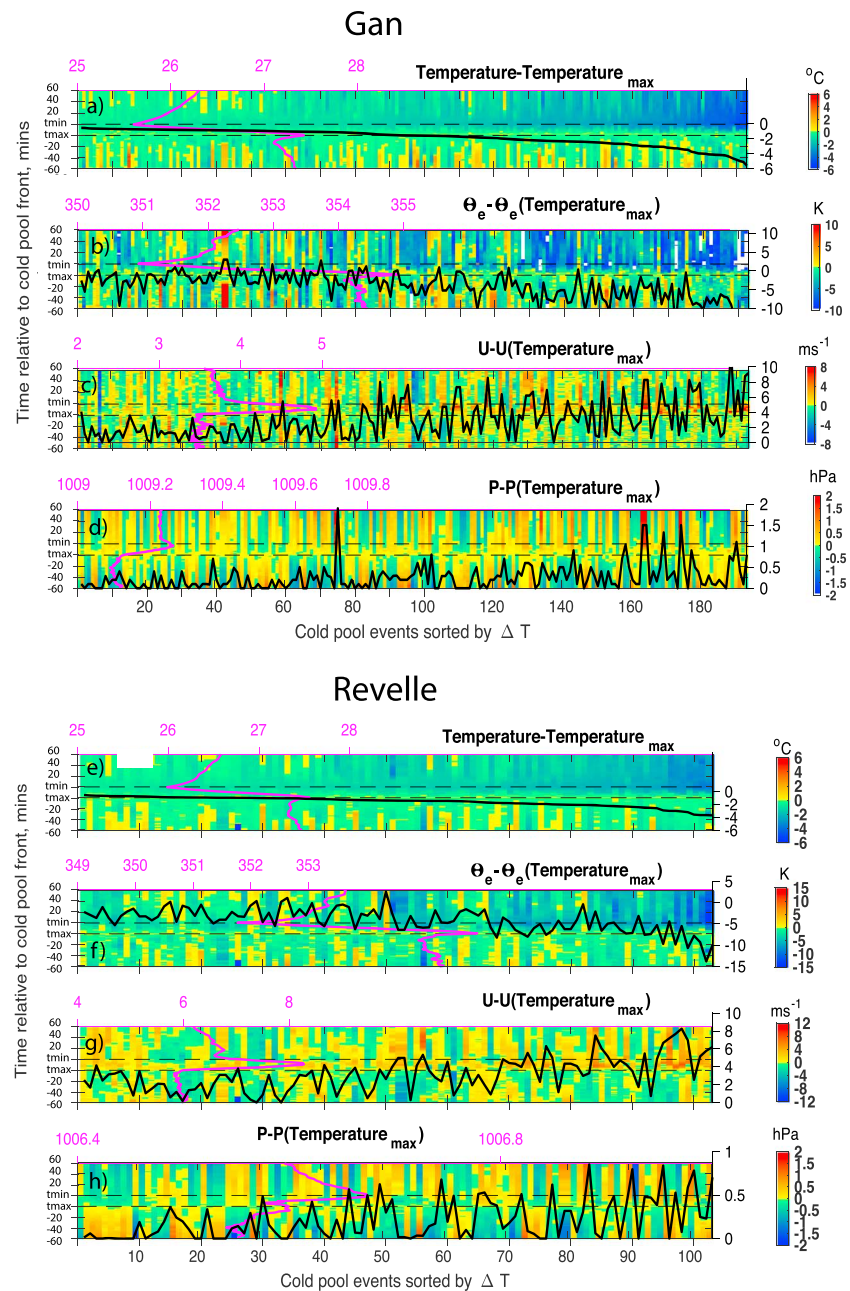
Figure 5. Cold pools sorted from small to large temperature decreases for (a, d) Gan Island and (e, h) *Revelle*. (a, e) Air temperature. (b, f) θ_e-θ_e at the time of the temperature maximum t_{max}. (c, g) Wind speed-wind speed at t_{max}. (d, h) Surface pressure-surface pressure at t_{max}. Difference values shown for 1 hr prior and post the cold frontal passage, with frontal passage values indicated through a black line, labeled on the right axes. t_{max} and t_{min} refer to location of the cold pool front edges. The composite average over all the cold pool events is indicated and labeled, both in magenta.

ues in the midtroposphere, corresponding to less moisture (Figure 6a). This mean θ_e profile is similar to that for the second-driest quartile when grouped by water vapor path (Figure 6b). If cold pools actively facilitate shallow-to-deep convection transitions through accessing drier air from the free troposphere, then the cold pools occurring during these MJO phases should be more pronounced. However, stronger or more numerous cold pools are not necessarily obvious in the observational time series during the more convectively suppressed time periods (Figure 3). An effort is made to statistically assess whether cold pool properties in nature are influenced by the overlying moisture distribution, by incorporating information about the CWV path above each cold pool. The water vapor path is a crude indicator of the moisture distribution within the
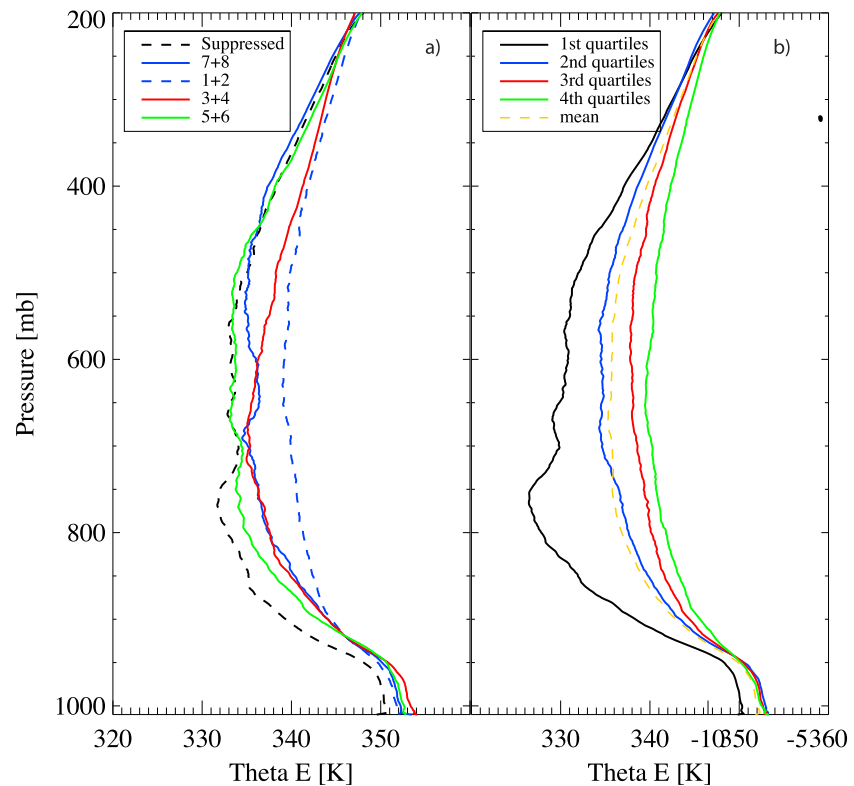
Figure 6. Mean profiles of equivalent potential temperature at Gan Island as a function of (a) Madden-Julian Oscillation phase (140 to 190 radiosondes per phase grouping) and (b) water vapor path quartile (190 radiosondes per quartile).

tropical atmosphere, in that increasing water vapor paths typically indicate a bottom-up moistening of the free troposphere (e.g., Figure 6 of Zhang et al., 2018). The water vapor path distribution above Gan Island has a mode at 5.2 cm, with the atmosphere saturating at slightly above 6 cm (Zhang et al., 2018). The change in the frontal passage of individual cold pools at Gan island, shown in Figure 7, includes color coding by their CWV path.

A systematic relationship between cold pool characteristics and CWV is unclear in Figure 7, although many of the stronger cold pools coincide with intermediate water vapor paths between 5 and 6 cm. Cold pools from the 7–14 October and 11–15 November time periods, indicated with triangles, are as likely to moisten the boundary layer as to dry it. This behavior is apparent in other cold pools as well. For many of these, θ_e remains conserved, indicating the downdraft air is originating from within the boundary layer. Weaker cold pools are associated with lower KAZR cloud top heights in Figure 8 of Zuidema et al. (2017), and the presence of truly shallow clouds during the convectively suppressed phases is previously noted (Benedict & Randall, 2007; Genio et al., 2012; Riley et al., 2011). Mild increases in θ_e may indicate a short-lived accumulation of surface fluxes within a newly formed shallow mixed layer (or may be a sampling issue). Changes in pressure are least correlated with the temperature decreases; we note large pressure gradients are not necessarily features of density currents (von Karman, 1940).

A time series sampling impartially at one point is indeed likely to sample many weak cold pools irrespective of the large-scale organization, because these are more numerous (e.g., Figure 5). Another approach focuses on the more pronounced cold pools and seeks to understand their larger-scale originating environment. Approximately 11 of the 193 original cold pools at Gan Island have decreases in the water vapor mixing ratio exceeding 2 g/kg, spanning a range of temperature decreases. Two additional examples of cold pools with q_v changes >2 g/kg, labeled 7 and 8, are included in Figure 7. As shown later, these are preceded by rain but are included to demonstrate a particular behavior. A total of eight examples of pronounced cold pools are numbered in Figure 7 and described in Table 1. Those chosen advect more directly over the AMF site, to avoid sampling at the cold pool edges (e.g., Tompkins, 2001). We turn to five of these examples to better understand how cold pools at Gan Island relate to the column moisture profile and the convective organization. All but one
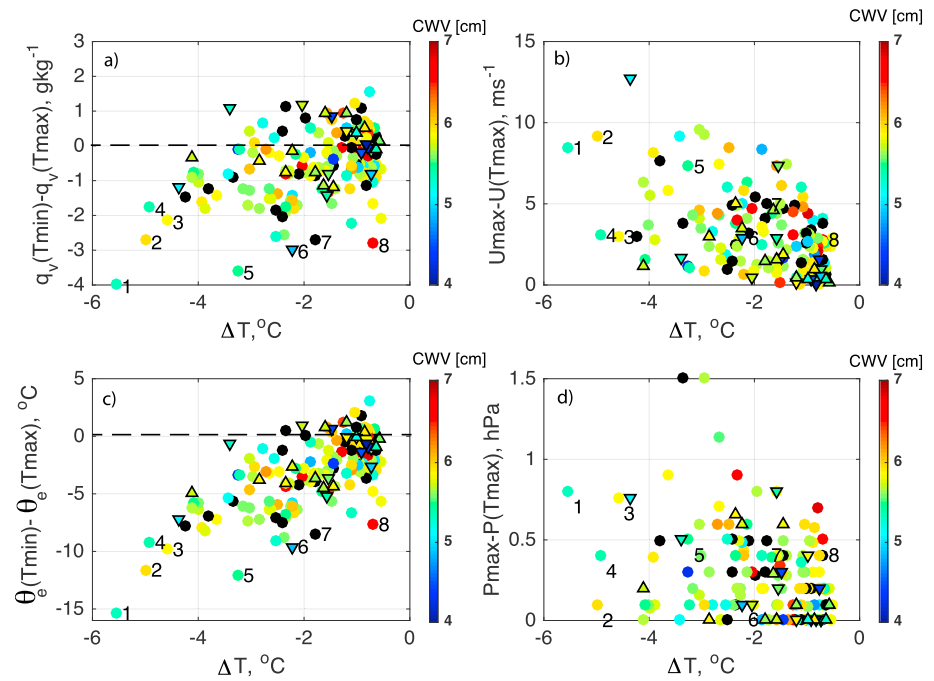
Figure 7. Changes across the cold pool fronts at Gan Island in (a) water vapor mixing ratio, (b) wind speed, (c) equivalent potential temperature, and (d) surface pressure, with color indicating the daily mean water vapor path. Numbered cold pools are detailed in Table 1. Cases 1, 2, 5, 7, and 8 are detailed in Figures 8 and 9. Downward-pointing and upward-pointing triangles correspond to the 7–14 October and 11–15 November suppressed time periods examined in Rowe and Houze (2015) and Ruppert and Johnson (2015). CWV = column water vapor.

(numbered 8 in Figure 7a) possess water vapor paths less than 6 cm. Taken together, these cases demonstrate that (a) the vertical humidity structure in which the convective downdrafts occur has an imprint on the subsequent near-surface air properties, (b) strong cold pools can be associated with cumulus only reaching the midtroposphere, (c) these cumuli are not truly isolated but are still organized into either lines or as mesoscale arcs around existing cold pools, and (d) wind speed increases in the composites correspond to gust fronts moving ahead of the spawning convection, which is more obvious when it is more organized into a line.

5. Case Studies of Strong Cold Pool Passages

Noteworthy is that six of the eight cold pools mentioned in Table 1 (#2 to #7) occur during MJO phases considered convectively suppressed (phases 4–8; Figure 3). One of the other two cold pools, though occurring during an MJO active phase on 31 October, is from a form of convective organization also more commonly associated with large-scale convective suppression, namely, a squall line. This cold pool produced the most pronounced decrease in both the surface temperature and humidity of all the 193 cold pools sampled at Gan Island stems (Figure 8). The 8 December cold pool (#2, also a strong cold pool) is also associated with a convective cloud line. The following five cases (#3 to #7) are cold pools from convection that appear isolated in the KAZR time series but whose spatial context reveals that they are organized around existing cold pools. Two of these (#6 and #7) coincide with the October time period documented within Ruppert and Johnson (2015) and Rowe and Houze (2015). Only the cold pool with the weakest temperature decrease, on 23 November, is associated with the stratiform precipitation typifying an MJO active phase and is characterized by an atmosphere that is moist throughout its entire depth (thermodynamic profile not shown but consistent with Figure 9a). This example (#8) is interesting in that the cold pool spawns from convection embedded within stratiform precipitation, and its cold pool passage registers a drying but little change in the surface temperature.

The changes in the surface layer properties caused by the five selected cold pools and their convective structure are shown in Figures 8 and 9, and the before- and after-cold-pool-front thermodynamic profiles from radiosondes in Figure 10. These individual cases are subsequently described following their order within Table 1.
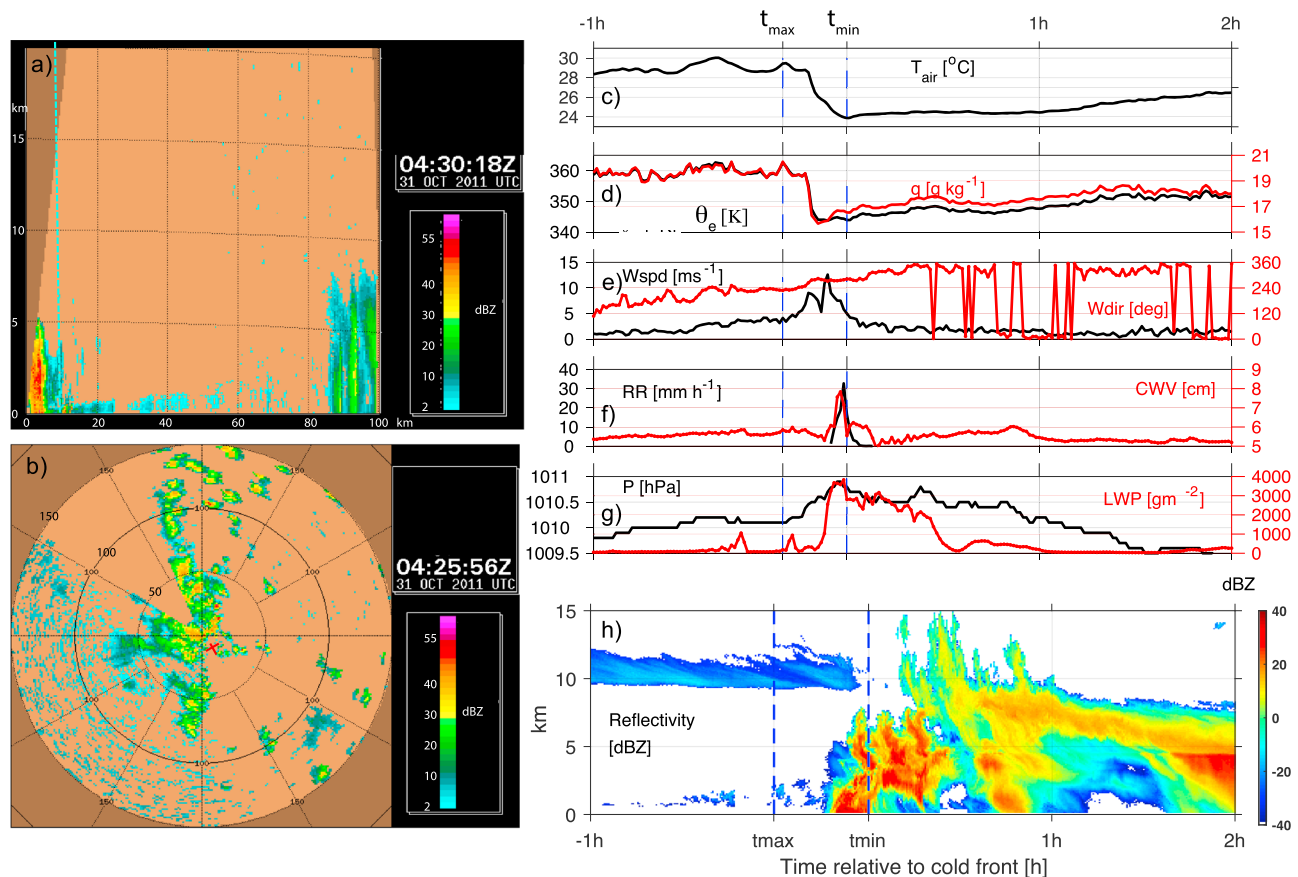
Figure 8. A squall line cold pool passing Gan Island on 31 October 2011, 4:30 UTC. (a) Shared Mobile Atmospheric Research and Teaching Radar range-height indicator image at an azimuth of 147° , directly above the AMF2 site. The squall line convection is located at the left side of the image. (b) a Shared Mobile Atmospheric Research and Teaching Radar horizontal cross section sampled at 4-km altitude shows the squall line structure. The squall line is moving west to east, and radii are indicated every 50 km. (c) Air temperature, (d) water vapor mixing ratio (red), and equivalent potential temperature (black), (e) wind speed (black) and direction (red), (f) RR (black, optical rain gauge), and CWV (red), (g) pressure (black), and LWP (red). (h) The 35-GHz zenith-pointing radar reflectivity. t_{max} and t_{min} denote the times with the maximum and minimum air temperatures demarcating the frontal passage (4:05 UTC and 4:19 UTC, respectively), normalized to span 20 min to be consistent with the composites. At t_{min}, precipitation and cloud is fully attenuating the KAZR and cloud above 8 km is not documented. CWV = column water vapor; LWP = liquid water path; RR = rain rate.

5.1. 31 October 4:25 UTC (#1): Squall Line

The main lesson from this example is that the temporal structure of its cold pool passage is the same as in the composites (Figure 4), if more pronounced. The spawning convection is capable of reaching the middle troposphere because the convection is organized in a line, helping to insolate it from entrainment drying. A temperature drop of 4 K demarcates the cold pool front, during which q_v decreases by 3 g/kg and θ_e decreases by 14 K. The wind speed increases coincide with the beginning of the cold pool front, with the rain occurring after the maximum in the wind gust. This indicates the cold pool density current is spreading out in front of the convective cloud line — a temporal structure also evident in the composites (Figure 4). The precipitation stems from a squall line with precipitation radar reflectivities reaching 55 dBZ up to 5 km (Figure 8a), and the 35-GHz cloud radar time-height series indicates cloud reaching at least 12 km when not attenuated (Figure 8h), trailed by stratiform cloud and precipitation. The winds thereafter settle back to the weak ~1 m/s pre-squall wind speeds. In contrast, the air temperature and water vapor mixing ratio do not recover to pre-cold-pool values until 6 hr after the cold pool front passage (not shown), with q_v recovering faster than the temperature. The surface pressure increases by almost 1 hPa for an hour after the cold pool (Figure 8f), consistent with a deep layer of cooling and condensate loading (Figure 8h). This is matched by radiosondes that reveal a dry layer above 2 km prior to the cold pool (Figure 10i). The deep layer drying is evident in a slight reduction in the CWV path of approximately 0.4 cm (Figure 8f, compare before- to after-cold-pool passage CWV). In the University of Washington daily summary, the National Center for Atmospheric Research SPol radar simultaneously
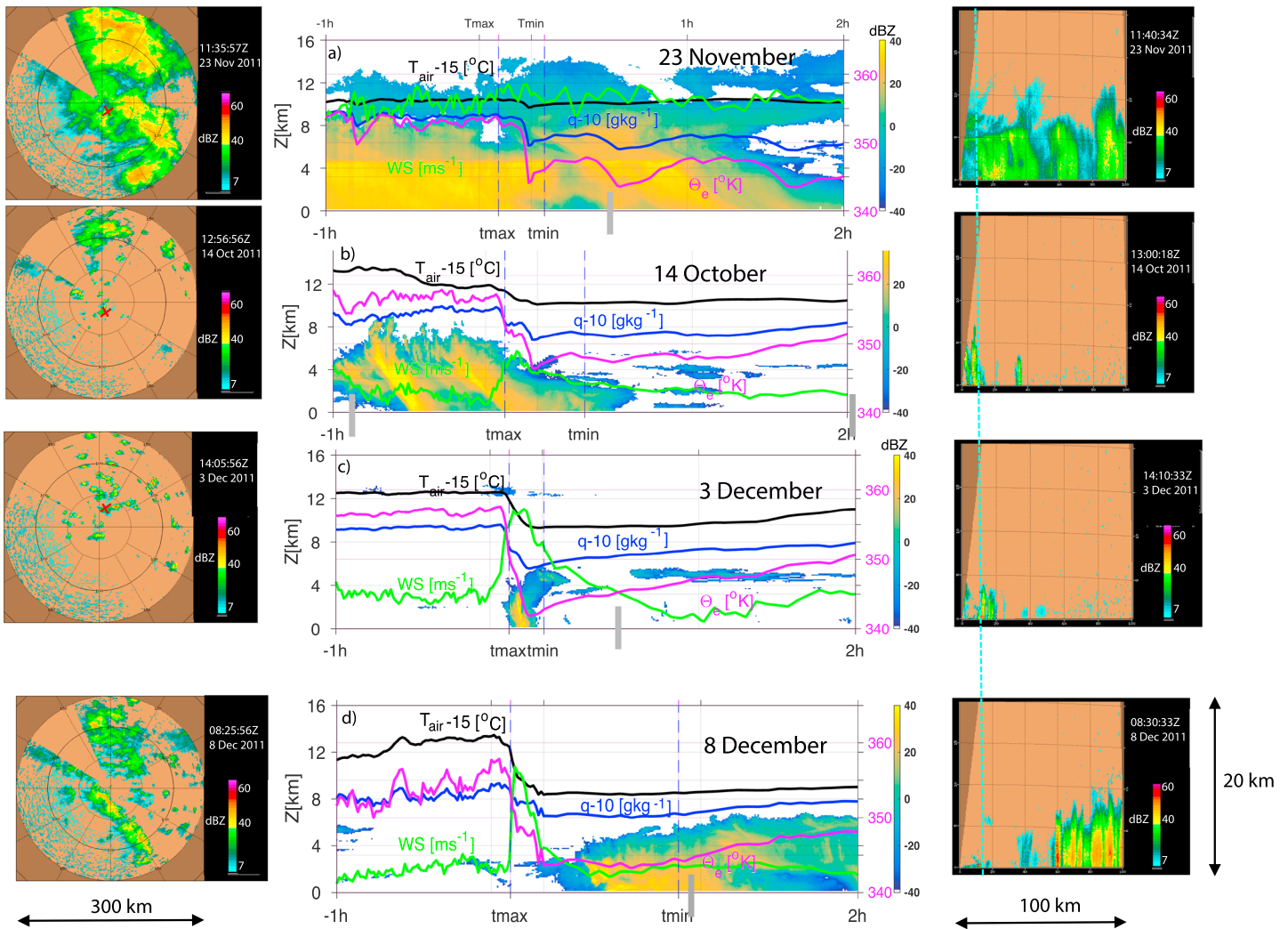
Figure 9. Shared Mobile Atmospheric Research and Teaching Radar surveillance scans (left panels), range-height indicator slices above the AMF site (right panels), and time series of K-band zenith-pointing cloud radar reflectivity profiles, surface air temperature (black), specific humidity (blue), equivalent potential temperature (pink), and wind speed (green) at the AMF site (middle panels) corresponding to the cold pools from (a) 23 November: 11:16 UTC, (b) 14 October: 12:28 UTC, (c) 3 December: 13:55 UTC, and (d) 8 December: 08:24 UTC, (i.e., cases 8, 7, 5, and 2, respectively). The actual values of temperature and specific humidity values are reduced by 15 ° C and 10 g/kg, respectively, to fit the scale. Short thick gray vertical lines on the time axis indicate approximate time of soundings depicted in Figure 10. Scales for the Shared Mobile Atmospheric Research and Teaching Radar images are indicated on the bottom panel. Radar reflectivities span from 2 to 66 dBZ, shown in more detail in Figure 8.

indicates rear-level inflow (not shown here). The slow temperature recovery is consistent with more cooling from evaporation of stratiform precipitation.

5.2. 8 December 8:30 UTC (#2): Long Convective Line

This cold pool (Figures 9d, 10g, and 10h) also originates from convection organized into a long line but, in this case, only reaches ~5 km and is unlikely to involve ice microphysics. The surface air temperature, moisture, and θ_e are rising prior to (east of) the passage of the cloud line for at least an hour, suggesting a large-scale surface convergence, though not of the scale documented for MJO propagation (Seo & Kim, 2003). A strong cold pool gust front approaching 10 m/s is located ahead (east) of the convective line, with air properties that reflect a convergence of both the before- and after-gust front air. Prior to the cold pool passage, the thermodynamic profile indicates enhanced water vapor mixing ratios below 1 km that can act to support convection (Figures 10g and 10h). That this cold pool passage is not as strong as in the previous 31 October case (Figure 8) is consistent with a pre-cold-pool thermodynamic profile that is more moist above 2 km and shallower convection. This day is also documented in Savarin et al. (2014) and Chen et al. (2016), who conclude from aircraft dropsondes that cold pools are both stronger and deeper during suppressed conditions than
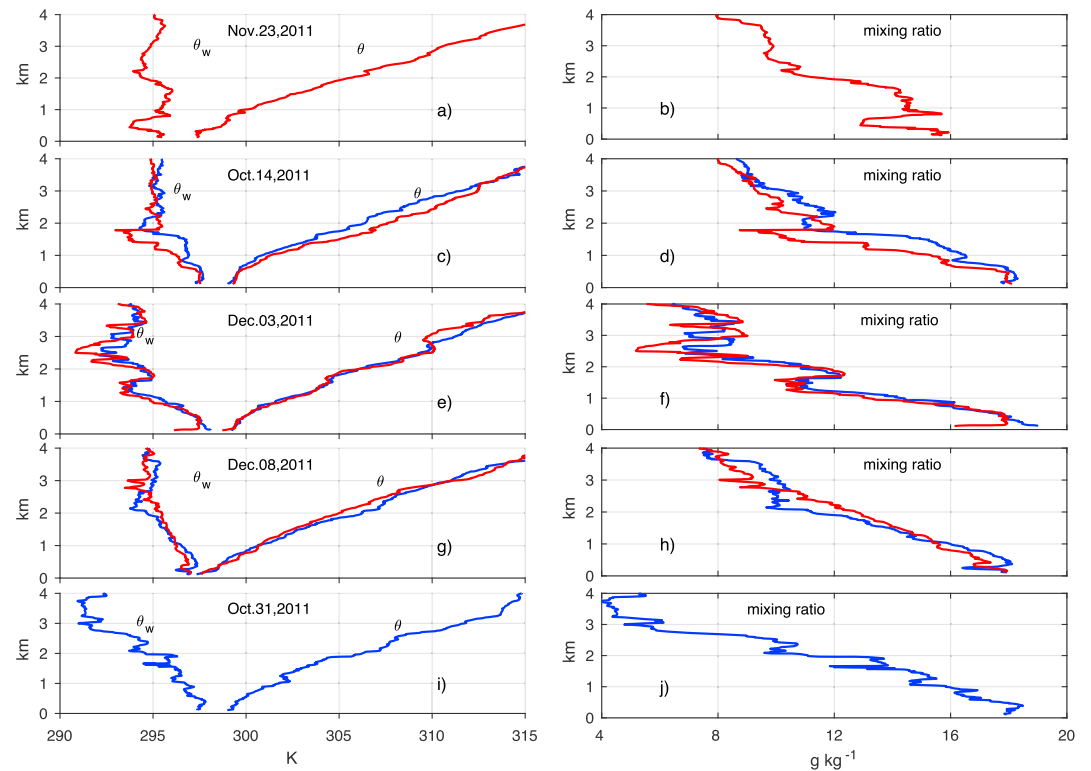
Figure 10. Profiles of potential temperature and wet bulb potential temperature (θ_w, left panels), mixing ratio (right panels) for (a, b) 23 November, (c, d) 14 October, (e, f) 3 December, (g, h) 8 December, and (i, j) 31 October. Blue and red curves represent before- and after-cold-pool frontal passage profiles from radiosondes released 0.89, 2.3, and 2.06 hr prior to the cold pool front in (c, e, g, and i) and 0.37, 2.1, 0.68, and 0.18 hr after the cold pool passage in (a, c, e, and g), indicated in Figure 9 when possible.

cold pools from days during more moist, convective phases. The cold pool strengths and depths correlated well with the low 700- to 500-hPa environmental relative humidities (Chen et al., 2016).

5.3. 3 December 14 UTC (#5): Isolated Convection

The 3 December cold pool (Figure 9c) is also representative of convection on 2 and 15 December (#3 and #4), in which nominally isolated clouds with tops reaching 5–6 km at best nevertheless produce strong cold pools. Convective lines, present in the morning, gave way to less-organized cold pools by this time. This particular cold pool produced the second-most surface drying, second only to 31 October but from a much more modest cloud type, explained by the presence of drier air at a lower altitude (compare the vapor mixing ratio at 1.5 km between Figures 10f and 10j). The gust front increases the surface wind speed by almost 10 m/s but just barely precedes the convection. The 12 UTC sounding shows dry air above 2 km, which the vigorous convection
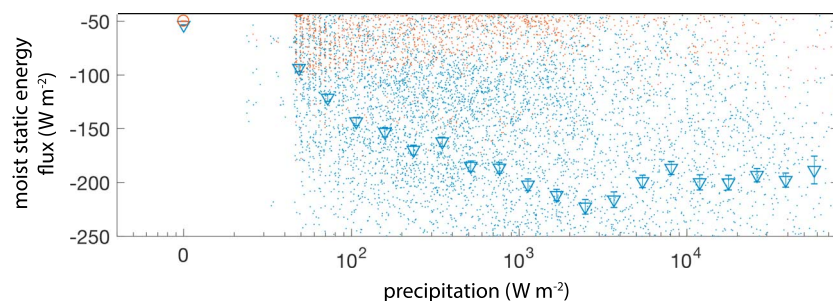
Figure 11. The boundary-layer moist static energy flux from downdrafts as a function of rain rate, based on flux tower observations from the *Revelle*, with the attribution methodology detailed in de Szoeke (2018). 1000 W m^{-2} of latent heating from precipitation is equivalent to a rain rate of approximately 1.44 mm hr^{-1}. Mean values are indicated with triangles.

Table 2
Correlations at 5-min Intervals Between the Root-Mean-Square Near-Surface Temperature Fluctuation (T′), Root-Mean-Square Near-Surface Wind Speed Fluctuation, or Gustiness (V′), Rain Evaporation Rate at 250-m Altitude ($\frac{\delta q_r}{\delta t}$), the Rain Mixing Ratio at 250 m (q_r), the Surface Precipitation Rate (P), and the Relative Humidity at 250 m (RH), Applied to SAM Simulations From October 2011 Centered on Both Gan Island and the Revelle

	T'	V'	$\frac{\delta q_r}{\delta t}$	q_r	P	RH_{250m}	M_d
T'	1.0	**0.92**	**0.90**	0.84	0.85	0.27	0.39
V'		1.0	0.82	0.74	0.75	0.04	**0.49**
$\frac{\delta q_r}{\delta t}$			1.0	**0.96**	**0.95**	**0.41**	0.14
q_r				1.0	0.99	**0.47**	0.14
P					1.0	0.45	0.15
RH_{250m}						1.0	**−0.48**

Note. Select relationships are highlighted with a bold font.

would have been able to access. The post-cold-front sounding 40 min after the cold front passage still indicates a shallow surface mixed layer, but the surface air mostly recovers within the 2 hr depicted, and the thermodynamic profile above 500 m returns to pre-cold-pool conditions, reflective of the smaller-scale convection. A trailing stratiform cloud near 4 km overlies the cold pool, altering both the shortwave and longwave radiative balance, a feature also evident in the next case discussed.

5.4. 14 October 13 UTC (#7): Convection at Cold Pool Boundary Encountering Dry Air Aloft
This cold pool (Figure 9b) is included, despite being preceded by rain, because it is a good example of a strong cold pool from a day similar to others from the 6–14 October time period, in that it contains multiple convective cells forming at cold pool boundaries (Rowe & Houze, 2015; Ruppert & Johnson, 2015). The rain preceeding the cold pool is also a good example of θ_e conservation from weakly driven convection, in which the temperature decreases slightly and the surface layer moistens. Large-scale drying is occurring above 1.5 km (Figure 10d). Despite this, the convection is able to reach 6–7 km. Most of the convection originates from the moister pre-cold-pool surface layer (compare Figure 10d to 10f and 10h), suggesting the gust front from a previous cold pool may have helped initiate the convection. The soundings occurring 1 hr prior and 2 hr post the cold pool front, primarily indicate a continued warming and drying above the boundary layer between 1–2 km after the isolated convection, reflecting a large-scale advection that is also apparent in Figure 14 of Zhang et al. (2018). The surface air mostly recovers within 2 hr, attaining a surface mixed-layer thickness of approximately 400 m. This is similar to the recovery of the 3 December cold pool. Trailing stratiform cloud at about 600 m, and 2- and 4-km altitude is consistent with liquid water path increases apparent in the cold pool composites (Figure 4) and would weakly alter the radiation balance. The time series prior to the cold pool front indicates.

5.5. 23 November 11:40 UTC (#8): Convection Embedded Within Stratiform Precipitation
This last example, also of a cold pool preceded by rain, occurred during an active MJO phase and provides a useful contrast to other examples. Strong drying during the cold pool passage is not accompanied by a strong temperature decrease. The strong cold pool emanates from a convective cell embedded within stratiform precipitation, one of many reported on the first truly rainy day of an MJO active phase. The convective cell is apparent in KAZR Doppler velocities that are not shown, but not in the cloud radar reflectivity time series, in which a bright band near 4 km persists even during the cold pool frontal passage (Figure 9a). Neither the temperature nor the wind speed change much during the drying associated with the cold pool edge. The sounding occurring 20 min after the cold pool passage samples a drier layer between 500 and 800 m and above 2 km (Figure 10a). An earlier 6-UTC sounding reveals the remnant of a deeper *onion* sounding (not shown), in which mesoscale sinking produces a downward vertical displacement that maintains the potential temperature, dries the air, but does not reach the surface (Zipser, 1977). Although speculative, the strong initial drying in this cold pool could reflect a downdrafting of air originally dried not far above by the slower mesoscale descent but accessed by this locally produced convective cell.

In the 31 October (Figure 8) and 8 December convective lines, the convection remains within the drier air mass but is fed by the moister air the convective line is moving into. That the strongest surface temperature
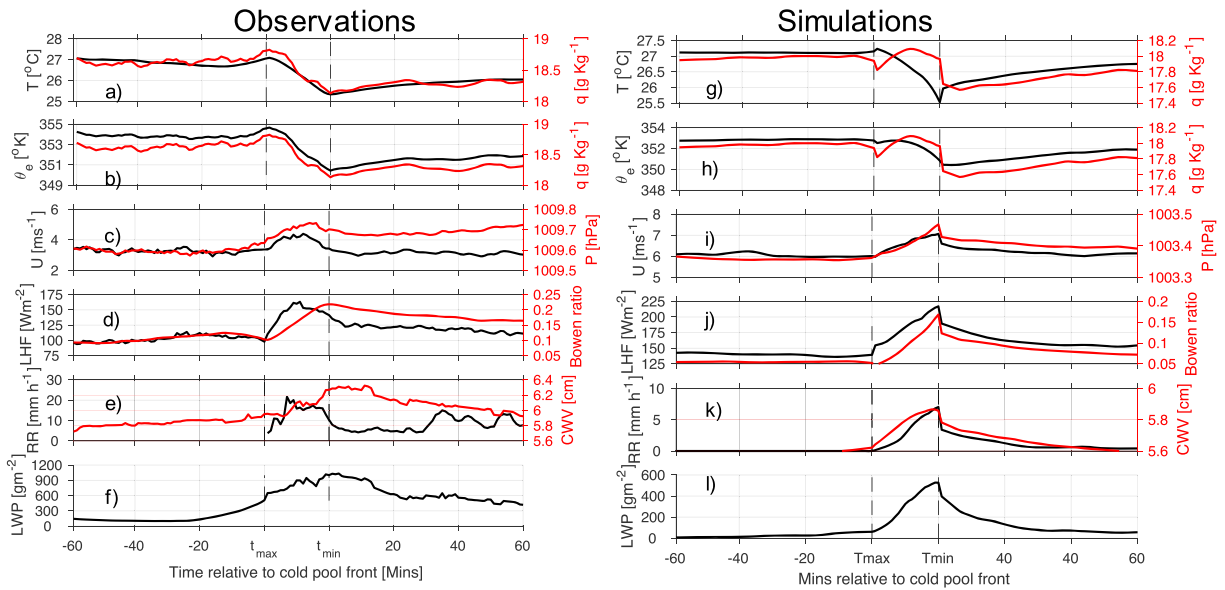
Figure 12. (left) Gan Island observations. (right) Gan Island System for Atmospheric Modeling simulations. 8–16 October 2011 and 18–25 December 2011 only. CWV = column water vapor; LHF = latent heat flux; LWP = liquid water path; RR = rain rate.

decreases are associated with such convective lines attests to the ability of more organized convection to survive within overall drier environments (Mapes et al., 2017), through a convective clustering that discourages the lateral entrainment of the drier air in at least one dimension. In the 23 November, 14 October, and 3 December cases, the convective clouds are located inside the more moist air masses, with the subsequent cold pools demarcated by less active convection (23 November) or none at all but containing residual cloud (14 October and 3 December). These cases may be secondary convection spawned by the gust front, with the parent convection no longer visible. The five examples described here support the idea that drier midtropospheres support stronger cold pools. Within the larger statistical sample of Figure 7, these cases support the idea that environments with intermediate column-integrated moisture values can sustain strong cold pools and are consistent with the observation made within Ciesielski et al. (2017) that periods with increasing rainfall tend to possess dry midlevels.
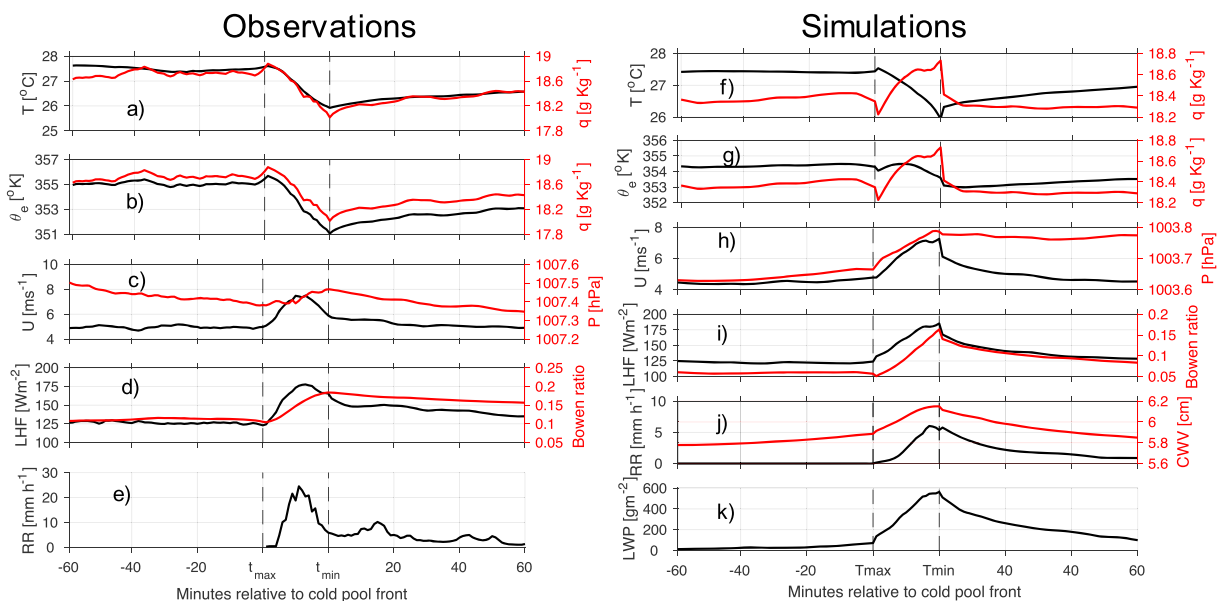
Figure 13. (left) *Revelle* observations. (right) *Revelle* System for Atmospheric Modeling simulations. 2 October to 1 November 2011 only. CWV = column water vapor; LHF = latent heat flux; LWP = liquid water path; RR = rain rate.
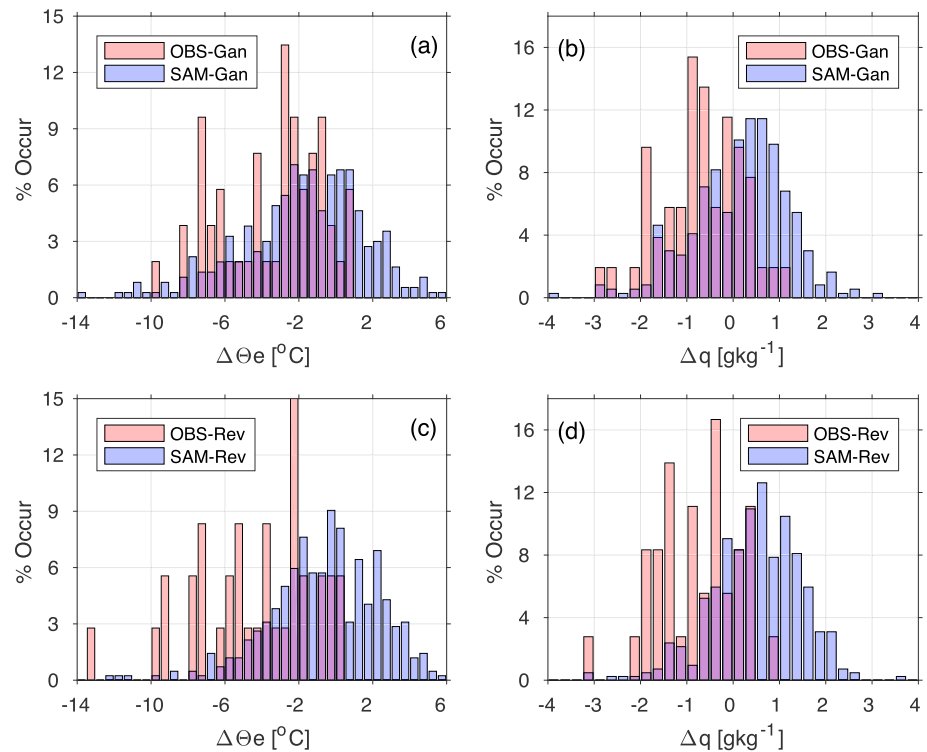
Figure 14. Observed and simulated (a) θ_e and (b) water vapor mixing ratio changes across cold pool fronts at Gan Island, 8–16 October 2011 and 18–25 December 2011 only. (c, d) Same as (a) and (b) but at the *Revelle* from 2 October to 1 November 2011. OBS = observation; SAM = System for Atmospheric Modeling.

Further support comes from Figure 11, in which the contribution to the boundary-layer moist static energy flux from downdrafts, as ascertained from flux tower measurements from the *Revelle*, is depicted as a function of rain rate. The conserved variables analysis by which the air properties are attributed to downdrafts is detailed in de Szoeke (2018). A notable feature is that as the precipitation increases to approximately 2,000 W/m², the moist static energy flux from downdrafts decreases approximately logarithmically, then levels off to a constant value of ~200 W/m². This is consistent with deeper updrafts being able to access drier midtropospheres and transport down drier air that can support more evaporation, before organized convection saturates the full free troposphere sufficiently that further evaporation near the surface is limited.

6. Analysis of Cloud-Resolving SAM Simulations

A further goal of this study is to assess if cloud-resolving simulations are able to capture the near-surface variability in cold pools documented in the composites. An initial analysis of the simulated cold pools quantifies the relationship between the model cold pool activity and physical processes relevant for creating the cold pools. The root-mean-square near-surface temperature fluctuation (T') measures the cold pool activity and is statistically related to the root-mean-square near-surface wind speed fluctuation, or gustiness (V'), the rain evaporation rate at 250-m altitude ($\frac{\delta q_r}{\delta t}$), the rain mixing ratio at 250 m (q_r), the surface precipitation rate (P), the relative humidity at 250 m (RH_{250m}), and the unsaturated convective downdraft mass flux at 250 m (M_d), shown in Table 2. The temperature fluctuations are most strongly correlated to the gustiness and rain evaporation rate, with the latter much more strongly correlated to the precipitation rate than to the relative humidity. The gustiness is positively correlated with the convective downdraft mass flux. Rain evaporation is positively correlated to the relative humidity, while the convective downdrafts are negatively correlated to the relative humidity. This suggests a casual link in which the rain evaporation increases the relative humidity, and the convective downdrafts reduce the relative humidity. In all, the correlations suggest sensible model simulations of the cold pools and that incorporating a *gustiness* parameter in climate models could be one method for cold pool parameterization.
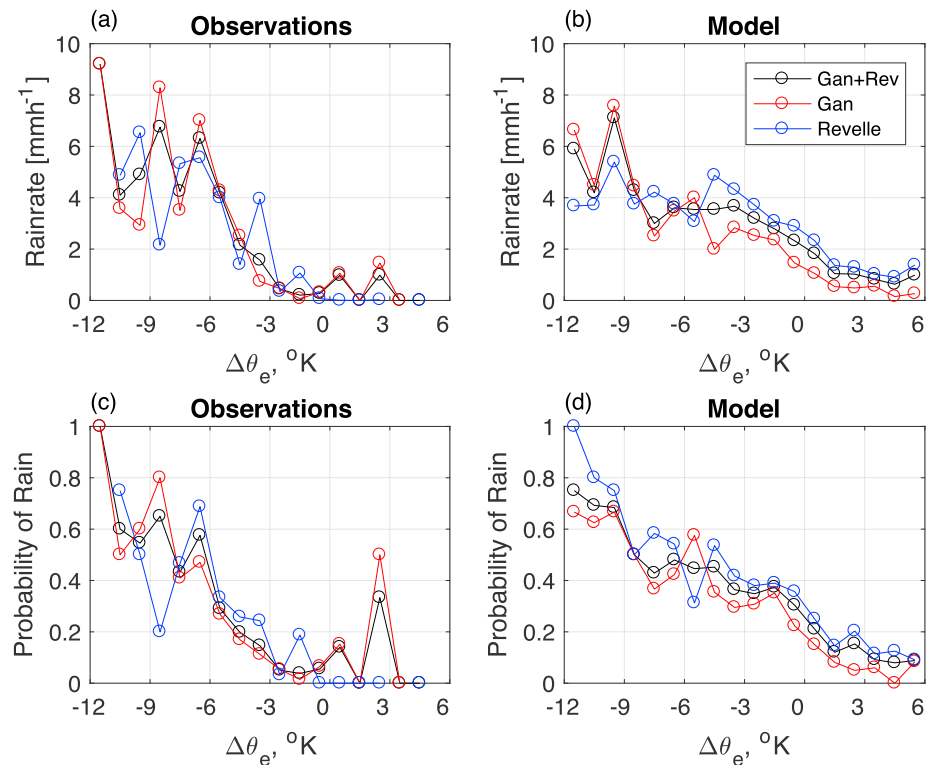
Figure 15. The hourly mean rain rate as a function of the θ_e change across the cold pool front from (a) observations and (b) the System for Atmospheric Modeling simulations. (c) The probability of precipitation (>2 mm/hr) for a given $\Delta\theta_e$ in the observations and (d) System for Atmospheric Modeling simulations. No rain criterion is imposed on the selected observed cold pools herein, generating a total of 779 (Gan) and 217 (*Revelle*) cold pools; 502 (Gan) and 585 (*Revelle*) cold pools are drawn from the simulations. The values from the simulations are 1 km^2 area averages while the observed values are point measurements. Rain rates of 0 contribute to the hourly mean averages.

The composites based on the SAM simulations, computed similarly to observational composites, (Figures 12, 13, portions of which are also shown in Figure 10 of Zuidema et al., 2017) show arguably similar relationships between the temperature decreases and gust fronts as in the observations. The same cannot be said for the moisture, however. In the observations, a slight increase in moisture occurs at the same time as the temperature increase, consistent with surface wind convergence. In contrast, in the simulations, the beginning of the cold pool front is accompanied with a slight drop in both moisture and θ_e, subsequently followed by an increase in q and θ_e. The increase in water vapor inside the cold pool edge resembles results from Tompkins (2001), in which water vapor accumulates within the outer one third of the cold pool. The attribution was to rain evaporation, consistent with the interpretation of the SAM simulations based on Table 2. The DYNAMO cold pool simulations analyzed in Feng et al. (2015) also indicate an increase in water vapor mixing ratio during cold pool passages (their Figure 3b). The differences in the change in moisture and associated change in θ_e across the cold pool fronts for the observations and simulations are summarized in Figure 14.

Anomalous moisture located inside the cold pool edge encourages an attribution to rain evaporation or surface fluxes (e.g., Langhans & Romps, 2015; Tompkins, 2001; Torri & Kuang, 2016) while anomalous moisture located outside the cold pool edge is more suggestive of a residual from a previous convective event and/or surface wind convergence (e.g., Li et al., 2014; Schlemmer & Hohenegger, 2016). While perhaps seeming minor, the disagreement between the model simulations of the moisture evolution with the observations suggest different processes for subsequent convection. The observations support the view that secondary convection is best able to thrive when anomalous environmental moisture accumulates independently nearby existing convection, most clearly evident for the convective lines on 31 October and 8 December, in which the cold pool density currents converge and mix with warmer, moister air outside the cold pool.

Additional insight stems from a metric introduced by Schiro and Neelin (2018). In Figure 15, the mean rain rate and the probability of rain exceeding 2 mm/hr are conditionally averaged by the change in θ_e ($\Delta\theta_e$) across

the cold pool front. Both the observations and simulations indicate that larger $\Delta\theta_e$ decreases coincide with higher rain rates. This indicates a close if unsurprising connection between the updrafts and downdrafts, in which stronger updrafts, generating deeper clouds, produce more rain and stronger downdrafts. Such behavior is evident in tethered balloon observations (Addis et al., 1984) and modeling studies (Jeevanjee & Romps, 2015); higher KAZR cloud top heights at Gan Island are also associated with stronger cold pools in Figure 8 of Zuidema et al. (2017). The increase in rain rate with negative $\Delta\theta_e$ may be sharper in the observations than in the simulations, but it is unclear if this is statistically significant. This feature may also reflect spatial averaging of the rain rates over the 1 km^2 model grid boxes, while the observed rain rates represent point values (Schiro & Neelin, 2018). More clear is that small changes in θ_e ($|\Delta\theta_e| \leq 3$ K) are more likely to occur with rain in the simulations than in the observations. Figure 14 further indicates how much more prevalent positive $\Delta\theta_e$ changes are in the simulations than in the observations. Both these features suggest that more of the convective downdrafts in the simulations have lower origin altitudes than in nature or the same model downdrafts mix more with environmental air than in nature. Conversely, the observations suggest that the updraft/downdraft dynamics present in nature are either stronger or more coherent (or both) than in the model.

7. Discussion and Implications

This study emphasizes using observations of approximately 300 cold pools to understand how cold pools are related to the atmospheric moisture distribution and the parent convection, coupled with a simultaneous evaluation of cloud-resolving simulations colocated in time and space. The study is relevant for understanding the role of cold pools as a key process affecting tropical cloud and rain mesoscale organization, and for guiding parameterization development of cold pools for global climate models. The observational analysis clarifies the connection between cold pool strength (the magnitude of the temperature decrease) to the decrease in θ_e, the latter being more connected in a more complex way to the structure of the thermodynamic profile, origin altitude, and mixing with environmental air. Through associating the cold pool characteristics with the CWV path (Figure 7) and connecting the more pronounced cold pools to the parent convection (Figures 8 and 9), clear examples are objectively identified of strong cold pools that result from seemingly isolated convection that only reach the midtroposphere, if the midlevels are dry. The two strongest cold pools, based on their temperature decrease, stem from more organized linear convection embedded within a drier atmosphere. The examples combined also make clear though that isolated cumuli reaching a dry midtroposphere are likely not really isolated, but part of a mesoscale organization, in the form of arcs and lines, that encourage a clustering, facilitated by the cold pools, that allow the cumuli to maintain themselves at the edge of moister boundary layers. The case studies also suggest stronger near-surface cold pools are more apparent in the convectively suppressed phases of the MJO.

Cumulus congestus are common in the Tropics, with Johnson et al. (1999) noting that cumulus congestus constituted half of the precipitating convective clouds sampled by shipboard radar in their study. Cumulus congestus are identified more strongly with convection suppression in the Tropics (e.g., Riley et al., 2011). The very definition of Cumulus congestus suggests strong updrafts within dry environments: "markedly sprouting clouds, often of great vertical extent, with a bulging upper that frequently resembles a cauliflower" (World Meteorological Organization, 1956). Through examining the mesoscale environment of cold pools, it becomes clear that it is highly likely that the tropical cumulus congestus, in nature, are strongly aided by cold pool dynamics whose signature is most easily seen in satellite or radar imagery as mesoscale arcs (e.g., Zuidema et al., 2003) rather than occurring in isolation.

A cold pool from a more active MJO phase provided an interesting counter example and spawns from convection embedded within stratiform precipitation. These are more likely to be weak because the near-surface air is already cooler and more saturated, as evident in the 23 November example (section 5.5) and seen statistically in de Szoeke et al. (2017). The boundary layer may also be less likely to fully recover before being subjected to the next cold pool in such conditions. This is also consistent with a boundary layer moist static energy budget analysis that links larger increases in the contribution from convective downdrafts to higher rain rates but only up to a maximum rain rate. Given that such individual cold pools are dwarfed in size relative to the mesoscale convective systems they are embedded in, it seems unlikely that the cold pools further influence the convective spectrum.

A direct comparison to the cold pools from one set of cloud-resolving simulations finds that model changes in the surface wind speeds during cold pool passages are realistic, but changes in the near-surface moisture distribution are less so, with moisture increasing inside the cold pool near the edge before dropping off toward the center (Figure 13), similar to results shown in Tompkins (2001). This is contrary to the observations. A correlation analysis attributes the moisture increase primarily to rain evaporation. A conditional averaging of rain rate by the change in θ_e (Figure 15), coupled with an assessment of the distribution in θ_e changes across the cold pool front (Figure 14), is consistent with an interpretation of either a lower altitude origin for the downdrafts in the models or more pronounced mixing with environmental air, compared to the observations. The convective downdrafts do dry the boundary layer air, but not enough, with the evaporation of the rain overcompensating. This occurs despite a microphysical scheme that has produced reasonable cold pools in previous studies (Li et al., 2014, 2015), suggesting other causes. The downdrafts were not found to be sensitive to the model horizontal grid spacing in a previous experiment (Zuidema et al., 2017). Other model processes that affect the behavior of cold pools include the entrainment of environmental air during both updrafts and downdrafts (e.g., Schiro & Neelin, 2018,Tompkins & Semie, 2017), as well as entrainment at gust front edges. Accurate simulations of the tropical environment within global climate models benefit from realistic representations of the downdrafts as well as the updrafts (Genio et al., 2012; Maloney & Hartmann, 2001; Sahany & Nanjundiah, 2008). Further emphasis on combined observational modeling interrogation of cold pool behavior in the Tropics at grid spacings able to more fully resolve the cold pool mixing processes is suggested.

References

Addis, R. P., Garstang, M., & Emmitt, G. D. (1984). Downdrafts from tropical oceanic cumuli. *Boundary-Layer Meteorology*, *28*, 23–49.

Banzon, V., Smith, T. M., Chin, T. M., Liu, C., & Hankins, W. (2016). A long-term record of blended satellite and in situ sea-surface temperature for climate monitoring, modeling and environmental studies. *Earth System Science Data*, *8*, 165–176.

Barnes, G. M., & Garstang, M. (1982). Subcloud layer energetics of precipitating convection. *Monthly Weather Review*, *110*, 102–117.

Benedict, J. J., & Randall, D. A. (2007). Observed characteristics of the MJO relative to maximum rainfall. *Journal of the Atmospheric Sciences*, *64*, 2332–2354. https://doi.org/10.1175/JAS3968.1

Bogenschutz, P. A., & Krueger, S. K. (2013). A simplified pdf parameterisation of sub grid-scale clouds and turbulence for cloud-resolving models. *Journal of Advances in Modeling Earth Systems*, *5*, 195–211. https://doi.org/https://doi.org/10.1002/jame.20018

Chandra, A., Zhang, C., Kollias, P., Matrosov, S., & Szyrmer, W. (2015). Automated rain rate estimates using the Ka-band ARM zenith radar (KAZR). *Atmospheric Measurement Techniques*, *8*, 3685–3699. https://doi.org/10.5194/amt-8-3685-2015

Chen, S., Kerns, B., Guy, N., Jorgensen, D., Delanoe, J., Viltard, N., et al. (2016). Aircraft observations of dry air, ITCZ, convective cloud systems and cold pools in MJO during DYNAMO. *Bulletin of the American Meteorological Society*, *97*, 405–423. https://doi.org/10.1175/bams-d-13-00196.1

Ciesielski, P. E., Johnson, R. H., Jiang, X., Zhang, Y., & Xie, S. (2017). Relationships between radiation, clouds, and convection during DYNAMO. *Journal of Geophysical Research: Atmospheres*, *122*, 2529–2548. https://doi.org/10.1002/2016JD025965

de Szoeke, S. (2018). Variations of the moist static energy budget of the tropical Indian Ocean atmospheric boundary layer. *Journal of the Atmospheric Sciences*, *75*, 1545–1551. https://doi.org/10.1175/jas-d-17-0345.1

de Szoeke, S., Skyllingstad, E. D., Zuidema, P., & Chandra, A. (2017). Cold pools and their influence on the tropical marine boundary layer. *Journal of the Atmospheric Sciences*, *74*, 1149–1168. https://doi.org/10.1175/JAS-D-16-0264.1

Fairall, C. W., Bradley, E. F., Godfrey, J. S., Wick, G. A., Edson, J. B., & Young, G. S. (1996). Cool-skin and warm-layer effects on sea surface temperature. *Journal of Geophysical Research*, *101*, 1295–1308.

Fairall, C. W., Bradley, E. F., Rogers, D. P., Edson, J. B., & Young, G. S. (1996). Bulk parameterization of air-sea fluxes for TOGA-COARE. *Journal of Geophysical Research*, *101*, 3747–3767.

Feng, Z., Hagos, S., Rowe, A. K., Burleyson, C. D., Martini, M. N., & de Szoeke, S. P. (2015). Mechanisms of convective cloud organization by cold pools over tropical warm ocean during the AMIE/DYNAMO field campaign. *Journal of Advances in Modeling Earth Systems*, *07*, 357–381. https://doi.org/10.1002/2014MS000384

Feng, Z., McFarlane, S. A., Schumacher, C., Ellis, S., Comstock, J., & Bharadwaj, N. (2014). Constructing a merged cloud-precipitation radar dataset for tropical convective clouds during the DYNAMO/AMIE experiment at Addu Atoll. *Journal of Atmospheric and Oceanic Technology*, *31*, 1021–1042. https://doi.org/10.1175/JTECH-D-13-00132.1

Fu, Q., Kruger, S. K., & Liou, K. N. (1995). Interactions of radiation and convection in simulated tropical cloud clusters. *Journal of the Atmospheric Sciences*, *52*, 1310–1328.

Genio, A. D. D., Chen, Y., Kim, D., & Yao, M.-S. (2012). The MJO transition from shallow to deep convection in CloudSat/CALIPSO data and GISS GCM simulations. *Journal of Climate*, *25*, 3755–3770. https://doi.org/10.1175/JCLI-D-11-00384.1

Genio, A. D. D., Wu, J., Wolf, A. B., Chen, Y., Yao, M.-S., & Kim, D. (2015). Constraints on cumulus parameterization from simulations of observed MJO events. *Journal of Climate*, *28*, 6419–6442. https://doi.org/10.1175/jcli-d-14-00832.1

Gottschalck, J., Roundy, P. E., Schreck, C. III, Vintzileos, A., & Zhang, C. (2013). Large-scale atmospheric and oceanic conditions during the 2011-12 DYNAMO Field Campaign. *Monthly Weather Review*, *141*(12), 4173–4196. https://doi.org/10.1175/MWR-D-13-00022.1

Grandpeix, J.-Y., & Lafore, J.-P. (2010). A density current parameterization coupled with Emanuel's convection scheme. Part I: The models. *Journal of the Atmospheric Sciences*, *67*, 881–897. https://doi.org/10.1175/jas3044.1

Jeevanjee, N., & Romps, D. M. (2015). Effective buoyancy, inertial pressure and the mechanical generation of boundary layer mass flux by cold pools. *Journal of the Atmospheric Sciences*, *72*, 3199–3213. https://doi.org/10.1175/jas-d-14-0349.1

Johnson, R., Rickenbach, T., Rutledge, S. A., Ciesielski, P., & Schubert, W. (1999). Trimodal characteristics of tropical convection. *Journal of Climate*, *12*, 2397–2418.

Khairoutdinov, M., & Randall, D. (2003). Cloud resolving modeling of the ARM summer 1997 IOP: Model formulation, results, uncertainties and sensitivities. *Journal of the Atmospheric Sciences*, *60*, 607–625.

Khairoutdinov, M., & Randall, D. (2006). High-resolution simulations of shallow-to-deep convection transition over land. *Journal of the Atmospheric Sciences*, *63*, 3421–3436.

Kingsmill, D. E., & Houze, R. A. (1999). Thermodynamic characteristics of air flowing into and out of precipitating convection over the west Pacific warm pool. *Quarterly Journal of the Royal Meteorological Society*, *125*, 1209–1229.

Langhans, W., & Romps, D. M. (2015). The origin of water vapor rings in tropical oceanic cold pools. *Geophysical Research Letters*, *42*, 7824–7834. https://doi.org/10.1002/2015GL065623

Li, Z., Zuidema, P., & Zhu, P. (2014). Simulated convective invigoration processes at trade-wind cumulus cold pool boundaries. *Journal of the Atmospheric Sciences*, *71*, 2823–2841. https://doi.org/10.1175/JAS–D–13–0184.1

Li, Z., Zuidema, P., Zhu, P., & Morrison, H. (2015). The sensitivity of simulated shallow cumulus convection and cold pools to microphysics. *Journal of the Atmospheric Sciences*, *72*, 3340–3355. https://doi.org/10.1175/JAS-D-14-0099.1

Long, C., Del Genio, A., May, P., Deng, M., McFarlane, S., Fu, X., et al. (2011). ARM MJO investigation experiment on Gan Island (AMIE-Gan) science plan (DOE/ARM Tech. Rep. DOE/SC-ARM-11-005, 63). U.S. Department of Energy.

Maloney, E. D., & Hartmann, D. L. (2001). The sensitivity of intraseasonal variability in the NCAR CCM3 to changes in convective parameterization. *Journal of Climate*, *14*, 2015–2034.

Mapes, B., Chandra, A. S., Kuang, Z., & Zuidema, P. (2017). Importance profiles for water vapor. *Surveys in Geophysics*, *38*, 1355–1369. https://doi.org/10.1007/s10712-017-9427-1

Morrison, H., Curry, J. A., & Khvorostyanov, V. I. (2005). A new double-moment microphysics parameterization for application in cloud and climate models. Part I: Description. *Journal of the Atmospheric Sciences*, *62*, 1665–1677.

Pei, S., Shinoda, T., Soloviev, A., & Lien, R.-C. (2018). Upper ocean response to the atmospheric cold pools associated with the Madden–Julian Oscillation. *Geophysical Research Letters*, *45*, 5020–5029. https://doi.org/10.1029/2018GL077825

Percival, D. B., & Walden, A. T. (2000). *Wavelet methods for time series analysis*. Cambridge, England: Cambridge University Press.

Powell, S. W., & R. A. Houze Jr (2013). The cloud population and onset of the Madden-Julian Oscillation over the Indian Ocean during DYNAMO-AMIE. *Journal of Geophysical Research: Atmospheres*, *118*, 11,979—11,995. https://doi.org/10.1002/2013JD020421

Randall, D. A., Xu, K., Somerville, R. J. C., & Iacobellis, S. (1996). Single-column models and cloud ensemble models as links between observations and climate models. *Journal of Climate*, *9*, 683–1697.

Reynolds, R. W., Smith, T. M., Liu, C., Chelton, D. B., Casey, K. S., & Schlax, M. G. (2007). Daily high-resolution-blended analysis for sea surface temperature. *Journal of Climate*, *20*, 5473–5496. https://doi.org/10.1175/jcli-d-14-00293.1

Riley, E. M., Mapes, B. E., & Tulich, S. N. (2011). Clouds associated with the Madden-Julian oscillation: A new perspective from CloudSat. *Journal of the Atmospheric Sciences*, *68*, 3032–3051. https://doi.org/10.1175/JAS-D-11-030.1

Rio, C., Grandpeix, J. Y., Hourdin, F., Guichard, F., Couvreux, F., Lafore, J. P., et al. (2013). Control of deep convection by sub-cloud lifting processes: The ALP closure in the LMDZ5B general circulation model. *Climate Dynamics*, *40*, 2271–2292. https://doi.org/10.1007/s00382-012-1506-x

Robert, A., Houze, Jr., & Betts, A. (1981). Convection in GATE. *Reviews of Geophysics*, *19*, 541–576.

Rowe, A. K., & Houze, R. A. Jr (2015). Cloud organization and growth during the transition from suppressed to active MJO convection. *Journal of Geophysical Research: Atmospheres*, *120*, 10,324—10,350. https://doi.org/10.1002/2014JD022948

Ruppert, J. H., & Johnson, R. H. (2015). Diurnally modulated cumulus moistening in the pre-set stage of the Madden-Julian Oscillation during DYNAMO. *Journal of the Atmospheric Sciences*, *72*, 1622–1647.

Sahany, S., & Nanjundiah, R. S. (2008). Impact of convective downdrafts on model simulations: Results from aqua-planet integrations. *Annales de Geophysique*, *26*, 1877–1887.

Savarin, A., Chen, S. S., Kerns, B. W., & Jorgensen, D. P. (2014). Convective cold pool structure and boundary layer recovery time in DYNAMO. In *Conference on Hurricanes and Tropical Meteorology* (9B.2 pp.). Boston, MA: American Meteorological Society.

Schiro, K. A., & Neelin, J. (2018). Tropical continental downdraft characteristics: Mesoscale systems versus unorganised convection. *Atmospheric Chemistry and Physics*, *18*, 1997–2010.

Schlemmer, L., & Hohenegger, C. (2014). The formation of wider and deeper clouds as a result of cold-pool dynamics. *Journal of the Atmospheric Sciences*, *71*, 2842–2858. https://doi.org/10.1175/JAS-D-13-0170.1

Schlemmer, L., & Hohenegger, C. (2016). Modifications of the atmospheric moisture field as a result of cold-pool dynamics. *Quarterly Journal of the Royal Meteorological Society*, *142*, 30–42. https://doi.org/10.1002/qj2625

Seo, K.-H., & Kim, K.-Y. (2003). Propagation and initiation mechanisms of the Madden-Julian Oscillation. *Journal of Geophysical Research*, *108*(D13), 4384. https://doi.org/10.1029/2002JD002876

Tompkins, A. M. (2001). Organization of tropical convection in low vertical wind shears: The role of cold pools. *Journal of the Atmospheric Sciences*, *58*, 1650–1672.

Tompkins, A. M., & Semie, A. G. (2017). Organization of tropical convection in low vertical wind shears: Role of updraft entrainment. *Journal of Advances in Modeling Earth Systems*, *9*, 1046–1068. https://doi.org/10.1002/2016MS000802

Torri, G., & Kuang, Z. (2016). Rain evaporation and moist patches in tropical boundary layers. *Geophysical Research Letters*, *43*, 9895–9902. https://doi.org/10.1002/2016GL070893

von Karman, T. (1940). The engineer grapples with nonlinear problems. *Bulletin of the American Mathematical Society*, *46*, 615–683.

Wheeler, M., & Hendon, H. H. (2004). An all-season real-time multivariate MJO index: Development of an index for monitoring and prediction. *Monthly Weather Review*, *132*, 1917–1932.

World Meteorological Organization (1956). *International cloud atlas*. Geneva, Switzerland: World Meteorological Organization.

Xie, S., Cederwall, R. T., & Zhang, M. (2004). Developing long-term single-column model/cloud system-resolving model forcing data using numerical weather prediction products constrained by surface and top of the atmosphere observations. *Journal of Geophysical Research*, *109*, 104. https://doi.org/10.1029/2003JD004045

Xu, W., Rutledge, S. A., Schumacher, C., & Katsumata, M. (2015). Evolution, properties, and spatial variability of MJO convection near and off the equator during DYNAMO. *Journal of the Atmospheric Sciences*, *72*, 623–640. https://doi.org/10.1175/JAS-D-15-0032.1

Yoneyama, K., Zhang, C., & Long, C. N. (2013). Tracking pulses of the Madden-Julian Oscillation. *Bulletin of the American Meteorological Society*, *94*, 1871–1891. https://doi.org/10.1175/bams-d-12-00157.1

Zhang, M. H., & Lin, J. L. (1997). Constrained variational analysis of sounding data based on column-integrated budgets of mass, heat, moisture, and momentum: Approach and application to arm measurements. *Journal of the Atmospheric Sciences*, *54*, 1503–1524. https://doi.org/10.1175/1520-0469(1997)054

Zhang, M., Lin, J. L., Cederwall, R., Yio, J. J., & Xie, S. C. (2001). Objective analysis of ARM IOP data: Method and sensitivity. *Monthly Weather Review*, *129*, 295–311. https://doi.org/10.1175/1520-0493(2001)129

Zhang, M. H., Somerville, R. C. J., & Xie, S. (2016). The scm concept and creation of arm forcing datasets. *Meteorological Monographs*, *57*, 24.1–24.12. https://doi.org/10.1175/AMSMONOGRAPHS-D-15-0040.1

Zhang, J., Zuidema, P., Turner, D., & Cadeddu, M. (2018). Surface-based microwave humidity retrievals over the equatorial Indian Ocean: Applications and challenges. *Journal of Applied Meteorology and Climatology*, *57*, 1765–1782. https://doi.org/10.1175/JAMC-D-17-0301.1

Zipser, E. J. (1977). Mesoscale and convective-scale downdrafts as distinct components of squall-line structure. *Monthly Weather Review*, *105*, 1568–1589.

Zuidema, P., Davies, R., & Moroney, C. (2003). On the angular radiance closure of tropical cumulus congestus clouds observed by the Multiangle Imaging Spectroradiometer. *Journal of Geophysical Research*, *108*, 4626–4641. https://doi.org/10.1029/2003JD003401

Zuidema, P., Li, Z., Hill, R., Bariteau, L., Rilling, B., Fairall, C., et al. (2012). On trade-wind cumulus cold pools. *Journal of the Atmospheric Sciences*, *69*, 258–277. https://doi.org/10.1175/jas–d–11–0143.1

Zuidema, P., Torri, G., Muller, C., & Chandra, A. (2017). A survey of precipitation-induced atmospheric cold pools over oceans and their interactions with the larger-scale environment. *Surveys in Geophysics*, *38*, 1283–1305. https://doi.org/10.1007/s10712-017-9447-x